Revista Geoaraguaia
ISSN:2236-9716
Barra do Garças – MT
v.11 n. Esp. Geotecnologias
p. 07-33. Ago-2021

INTRAURBAN ANALYSIS OF SURFACE URBAN HEAT ISLAND FROM DISAGGREGATED THERMAL RADIANCE IMAGES

ANÁLISE INTRAURBANA DE ILHAS DE CALOR DE SUPERFÍCIE A PARTIR DE IMAGENS DE RADIÂNCIA TERMAL DESAGREGADA

Vanessa da Silva Brum Bastos[1]

Leila Maria Garcia Fonseca[2]

Carolina Moutinho Duque de Pinho[3]

ABSTRACT

Surface Urban Heat Islands (SUHI) are areas with higher surface temperatures than their surroundings. Several studies have used thermal images from satellites to research the influence of urbanization on surface temperature patterns, however the low spatial resolution of thermal sensors limits the analysis of LST intraurban variations. Attempting to overcome this limitation, we used the Enhanced Physical Model (EPM) for disaggregation of land surface temperature (DLST) to generate fine scale LST for Sao Paulo city in Brazil. This method uses a linear regression and Planck's law to combine NDVI, NDWI and UI to estimate LST at finer spatial detail. First, we calibrate the method by upscaling an ASTER thermal band to 1000 m and using EPM to estimate the original 100 m thermal band. The original and estimated ASTER thermal bands achieved and R^2 of 0.66. Following, we apply the EPM model to estimate the LST at 15 m and compare it with data from meteorological stations. The 15 m LST image facilitated the identification of potential SUHIs. The EPM model provides an enhanced product with higher level of spatial detail, which allows researchers to identify changes of surface temperature that would not be evident from an ASTER LST (90 m spatial resolution) product. In summary, the model allowed us to quantify and map the influence of different urbanization patterns on the LST distribution.

Keywords: land surface temperature, thermal, disaggregation, surface urban heat island.

1 Research and Teaching Fellow na School of Geography and Sustainble Development - University of St. Andrews (United Kingdom). vdsbb@st-andrews.ac.uk ORCID: https://orcid.org/0000-0002-5865-0204

2 Pesquisadora do Instituto Nacional de Pesquisas Espaciais – INPE. leila@dpi.inpe.br ORCID: https://orcid.org/0000-0001-6057-7387

3 Professora do curso de Bacharelado em Planejamento Territorial da Universidade Federal do ABC (UFABC). carolina.pinho@ufabc.edu.br ORCID: https://orcid.org/0000-0002-7054-4463

Revista Geoaraguaia
ISSN:2236-9716
Barra do Garças – MT
v.11 n. Esp. Geotecnologias
p. 07-33. Ago-2021

RESUMO

Ilhas de calor de superfície (ICS)são áreas com temperatura de superfície maior do que as áreas ao redor. Vários estudos têm usado imagens termais de satélite para investigar a influência da urbanização nos padrões de temperatura de superfície, entretanto a baixa resolução espacial dos atuais sensores termais limita a análise dos padrões de variação intraurbana de temperatura de superfície. Com o objetivo de superar essa limitação, nós utilizamos o *Enhanced Physical Model* (EPM) para gerar dados de temperatura de superfície com maior nível de detalhamento para a cidade de São Paulo- Brasil. Esse método utiliza um modelo de regressão linear e a lei de Planck para combinar NDVI, NDWI e UI para estimar a temperatura de superfície com maior nível de detalhes espaciais. Primeiro, para calibrar o modelo, nós reamostramos uma banda termal ASTER para 1000 m e utilizamos o método EPM para estimar a banda original de 100 m. A banda termal reamostrada de 100 m atingiu um R2= 0.66 em relação a banda termal original. A seguir, nós aplicamos o método EPM para estimar a temperatura de superfície à 15 m. A imagem de temperatura de superfície de 15 m facilitou a identificação de potenciais ilhas de calor de superfície. O modelo EPM fornece um produto com alto grau de detalhamento espacial, o que permite que pesquisadores identifiquem as mudanças de temperatura de superfície que não seriam evidentes na imagem termal ASTER original (90 m de resolução espacial). Em suma, o modelo nos permitiu quantificar e mapear a influência de diferentes padrões de urbanização na distribuição dos padrões de temperatura de superfície.

Keywords: Keyword 1; Keyword 2; Keyword 3.

INTRODUCTION

Land Surface Temperature (LST), the radiative skin temperature of land surface, is a key modulator of the energy balance at the Earth's surface and plays a leading role on surface processes at multiple scales (KHANDELWAL et al., 2017b). LST influences a myriad of physical processes in the atmosphere, such as heat fluxes, air motion, humidity distribution, evapotranspiration and local atmospheric circulation; for this reason LST has been used for varied applications, such as estimate of soil humidity (MERLIN et al., 2012), detection of forestry fires (ECKMANN; ROBERTS; STILL, 2008), investigation of hydrological processes (CROW; WOOD, 2005; MCLAUGHLIN, 2002), exploring the relationship between disease vectors and urban heat islands (AZEVEDO et al., 2012), climatological studies (KUSTAS; ANDERSON, 2009) and monitoring urban surface heat islands (MEMON; LEUNG; CHUNHO, 2008; OGASHAWARA; BASTOS, 2012; ZHOU et al., 2011).

Revista Geoaraguaia
ISSN:2236-9716
Barra do Garças – MT
v.11 n. Esp. Geotecnologias
p. 07-33. Ago-2021

In climatology, LST is often used as a proxy for changes in heat distribution caused by land cover modification (GARTLAND, 2008; MONTEIRO, 1976; OKE, 1987; VOOGT; OKE, 2003). Since the 80's, urban climatology has been using thermal images to analyse LST distribution and its relationship with land cover changes at coarse to medium spatial scale (ANIELLO; MORGAN; NEWLAND, 1995; EFRAIN et al., 2013; KHANDELWAL et al., 2017a; MCMICHAEL et al., 2008; MEMON; LEUNG; CHUNHO, 2008; ROTH; OKE, 1989; TAN et al., 2010). LST daily and seasonal cycles have been studied using thermal images from meteorological satellites, and earth observation satellites like Terra and Aqua (MEMON; LEUNG; CHUNHO, 2008; TAN et al., 2010; YANG et al., 2011; ZHOU et al., 2011; ZHU; LŰ; JIA, 2013); but fine spatial scale LST analysis is still incipient because of the trade-off between spatial and temporal resolutions for thermal images (Table 1).

Table 1 – Satellites with thermal sensors on board and respective resolutions

Satellite/Sensor	Spatial resolution (m)	Temporal resolution
GOES/ I-M	4000	30 minutes
NOAA/ AVHRR	1100	6 hours
Terra & Aqua/MODIS	1000	2 days

Source: Authors (2021).

The analysis of LST at a finer scale could help improving our understanding of Urban Heat Islands (UHI) in big cities. UHI are a modification of heat distribution driven by changes in roughness and urban surface emissivity. Urban structures characteristically store more energy for longer durations, which consequently leads to increased local temperature. The temperature increase may cause humans thermal discomfort, economic and social losses, negative impacts to health, and damages to mental and physical efficiency (GARTLAND, 2008; MONTEIRO, 1976; OKE, 1987; VOOGT; OKE, 2003).

The investigation of the relationship between land cover and UHI originated with the development of the first orbital thermal sensors; however this work has primarily been dedicated to studying the general influence of urbanization on land surface temperature patterns (ANIELLO; MORGAN; NEWLAND, 1995; EFRAIN et al., 2013; KHANDELWAL et al., 2017a; MCMICHAEL et al.,

2008; MEMON; LEUNG; CHUNHO, 2008; ROTH; OKE, 1989; TAN et al., 2010). The general scope of these studies is partially a result of the trade-off between a satellites spatial and temporal resolution, especially for thermal sensors (Table 1). Finer spatial resolutions would enable the characterization of the relationship between each land cover class and its LST pattern.

Typically orbital sensors cannot distinguish intraurban objects, with the exception of a few high resolution sensors (World View II, Pleiades, Rapid Eye), which leads to a pixel mixing effect, i.e., the signal of multiple objects being recorded inside the same pixel (ZHAN et al., 2013). The mixture effect is inherent to the imaging process and is more pronounced for spectral bands with low signal/noise ratio (SNR). Thermal bands are characterized by a low signal to noise ratio, which is improved by integrating the signal over a bigger area, i.e., using a coarser resolution. Despite continued improvements in thermal sensors, the mixture effect remains with thermal orbital satellite images. In urban areas, the mixture effect is especially problematic, because urban objects are almost always smaller than what can be represented by the spatial resolution of these images.

In an effort to deal with the mixture effect, methods for disaggregation of land surface temperature (DLST), also known as downscaling methods, have been developed. DLST methods allow scientists to generate more spatially detailed thermal datasets by combining auxiliary datasets, statistical methods and/or concepts from physics. Methods for DLST have been applied to extract land surface temperature in urban environments (NICHOL; WONG, 2009), analyse urban heat island daily cycles (ZAKŠEK; OŠTIR, 2012), estimate thermal radiance (LIU; PU, 2008), and detect wildfire at the subpixel scale (DENNISON et al., 2006).

Several DLST methods have been proposed (BECHTEL; BÖHNER; WIESNER, 2013; ECKMANN; ROBERTS; STILL, 2008; KAWASHIMA, 1994; LIU; PU, 2008; LIU; ZHU, 2012; NICHOL; WONG, 2009; SZYMANSKI et al., 1999; YANG et al., 2010) but linear regression based methods (LIU; PU, 2008; LIU; ZHU, 2012) are the most computationally straightforward . They usually require one image in the visible spectrum, one near-infrared band, thermal infrared spectral bands and a land surface temperature product from same day and approximately same time.

Revista Geoaraguaia
ISSN:2236-9716
Barra do Garças – MT
v.11 n. Esp. Geotecnologias
p. 07-33. Ago-2021

The main objective of this research is to use a DLST model based on linear regression to generate more detailed LST images for urban areas and consequently be able to perform more detailed analyses on urban surface temperature patterns and Surface Heat Island (SUHI). The main advantages of the use of linear regression to develop the DLST model are its lower computational cost and possibility to perform further quantitative analyses of the accuracy of the resulting LST estimates. The DLST model we employ builds from model proposed by (LIU; PU, 2008) and we use it to analyse intraurban LST patterns and detect potential UHIs in the São Paulo municipality of Brazil.

BACKGROUND

URBAN HEAT ISLAND (UHI)

Changes in the spatial and temporal distribution of the air temperature and heat content are one of the most impactful climate phenomena for humans (GARTLAND, 2008). The UHI effect is defined as the increase of surface and air temperature in urban areas compared to surrounding rural areas (GARTLAND, 2008; OKE, 1987), or in a more general form, the positive temperature differential of a rural or green area from the urban area. UHI's are a result of changes on how energy is absorbed, reflected, and emitted by the Earth's surface (i.e., the energy balance), which are associated with urban development and structures (GARTLAND, 2008; OKE, 1987). These changes bias the liquid radiation balance, which is the difference between the income solar radiation and the radiation emitted back to outer space by Earth. Under ideal conditions, the Earth liquid radiation balance is positive during the night and negative during day and a thermal equilibrium is obtained. However, this equilibrium is not observed in many urban areas, which often results in an increasing trend in temperature from the urban periphery toward the downtown urban core (CLIMATE PROTECTION PARTNERSHIP, 2010; GARTLAND, 2008; LOMBARDO, 1985).

UHIs can be categorized as one of two types: Atmospheric UHI (AUHI), which have higher air temperatures than surrounding rural areas and Surface UHI (SUHI), which have higher surface temperatures than surrounding rural areas. Both AUHIs and SUHIs have different genesis, detection methods, mitigation strategies and intensity (Table 2).

Revista Geoaraguaia
ISSN:2236-9716
Barra do Garças – MT
v.11 n. Esp. Geotecnologias
p. 07-33. Ago-2021

Table 2 – Characteristics of SUHI and AUHI

Characteristic	Surface UHI	Atmospheric UHI
Period	During the entire day. More intense during the day and in summer.	Small or non-existent during the day. More intense during the night, at daybreak and in winter.
Intensity peak	Bigger spatial and temporal variation: Day: between 10°C and 15°C. Night: between 5°C and 10°C.	Smaller variations: Day: between -1°C and 3°C. Night: between 7°C and 12°C.
Detection methods	Indirect measurements: Remote Sensing.	Direct measurements: Meteorological stations; In situ measurements.
Representation methods	Thermal images.	Isotherms maps; Temperature graphs.

Source: Climate Protection Partnership, 2010 (modified).

Regardless of type, UHIs are harmful to the environment and decreases the quality of life for those living under it. UHIs accelerate chemical weathering, which degrades urban physical structures, increases energy consumption (e.g., for air conditioning), decrease water quality, undermine human comfort and health, and increase pollutants and greenhouse gas emissions (CLIMATE PROTECTION PARTNERSHIP, 2010; GARTLAND, 2008; LOMBARDO, 1985; OKE, 1987). In addition, UHI's can exacerbate heat waves and provide favourable conditions for the development of disease vectors (e.g., mosquito (AZEVEDO et al., 2012)), which can lead to an increase in disease transmission and mortality rates (HAJAT; KOSATKY, 2010; MCMICHAEL et al., 2008; TAN et al., 2010; WANG; HE; LIU, 2012).

STUDY AREA

The municipality of São Paulo lies within the state of São Paulo in the south-eastern part of Brazil (Figure 1). We selected the municipality of São Paulo, hereafter São Paulo, as our study area because it is one of the largest urban metropolitan areas in the world, and it has an urbanization rate of 99.10% (IBGE, 2010). São Paulo's climate is humid temperate with a dry winter and a warm summer (MENDONÇA; DANNI-OLIVEIRA, 2007); the average temperature is 15ºC for the coldest month and

22ºC for the warmest month. The average rainfall is between 39.mm for the driest month and 256.mm for the wettest month.

Figure 1 – Study area, the municipality of São Paulo is shown on an ASTER 3N(R)2(G)1(B) composition. The built-up area can be seen in shades of grey while red indicates the presence of vegetation.

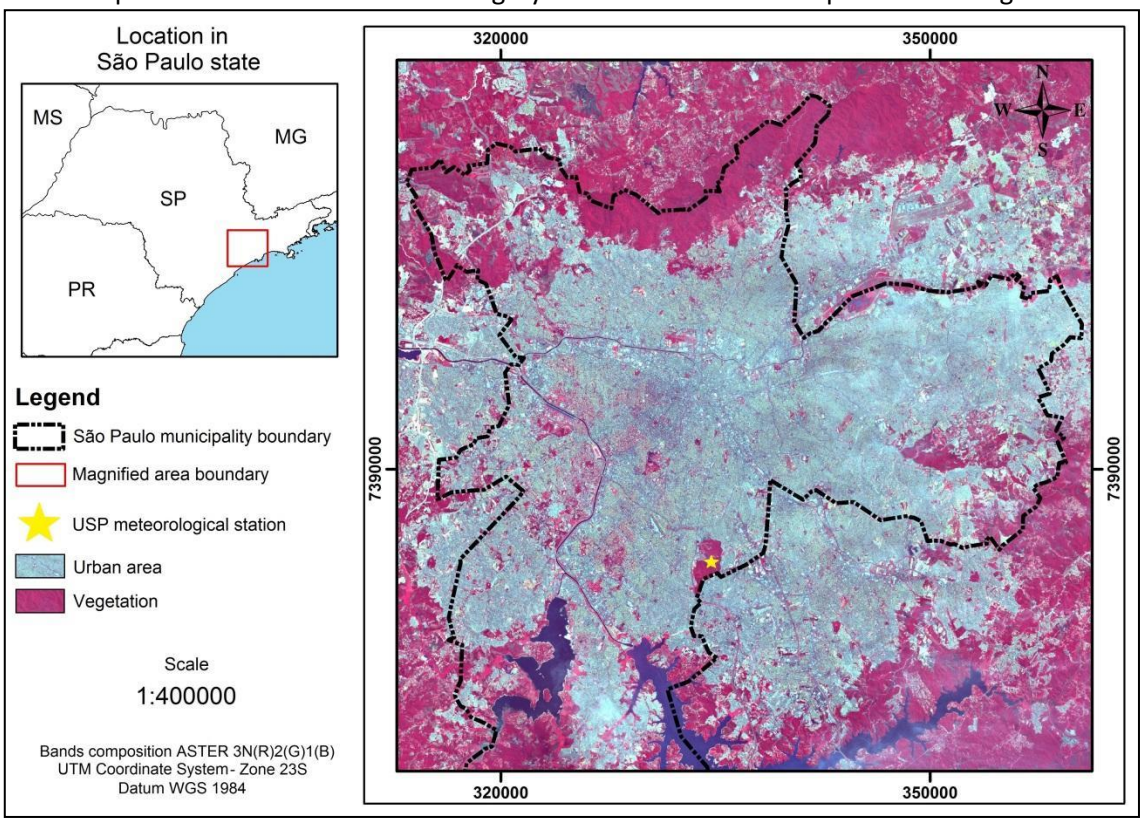

Source: Authors (2021).

METHODOLOGY

We applied a thermal unmixing DLST method, using one ASTER (Advanced Spaceborne Thermal Emission and Reflection Radiometer) image from 13th October 2002 taken at 10:30 am, the most recent date with valid Short Wavelength Infrared (SWIR) data available. We also used the MODIS (Moderate-Resolution Imaging Spectroradiometer) land surface temperature product from

the same date and approximately same time and daily temperature data from the University of São Paulo's (USP) meteorological station (Figure 1).

DATA PRE-PROCESSING

We corrected atmospheric effects and converted all 14 ASTER 1B bands from digital numbers (DN) to radiance, and subsequently to reflectance, using the FLAASH algorithm (Fast Line-of-sight Atmospheric Analysis of Spectral Hypercubes) (ADLER-GOLDEN et al., 1999) with the Mid-Latitude Atmospheric Model and Urban Aerosol Model, which is a mixture of 80% rural aerosol with 20% soot-like aerosols.

With the purpose of explaining temperature through other related environmental variables, we calculated three radiometric indices that address urban density, vegetation, and water content. For urban density we calculated the urban index (UI) (JAYAMANNA, 1996), which is based on the inverse relationship between the reflectance of urban areas in the near infra-red (NIR) and short wavelength infra-red (SWIR) bands.

$$UI = \frac{SWIR_{2.20\mu m} - NIR_{1.65\mu m}}{SWIR_{2.20\mu m} + NIR_{1.65\mu m}} \quad (1)$$

For vegetation we used the normalized difference vegetation index (NDVI) (ROUSE et al., 1973) that explores the inverse relationship of vegetation reflectance between NIR and Red bands.

$$NDVI = \frac{NIR_{1.65\mu m} - RED_{0.82\mu m}}{NIR_{1.65\mu m} + RED_{0.82\mu m}} \quad (2)$$

For water content we modified the normalized difference water index (NDWI) (GAO, 1996) to adapt it to ASTER spectral bands. The modification was necessary because ASTER imagery does

Revista Geoaraguaia
ISSN:2236-9716
Barra do Garças – MT
v.11 n. Esp. Geotecnologias
p. 07-33. Ago-2021

not include a band centred on 1.24 µm and the band centred on 2.26 µm is also free of water absorption.

$$NDWI = \frac{RED_{0.82\mu m} - SWIR_{2.26\mu m}}{RED_{0.82\mu m} + SWIR_{2.26\mu m}} \quad (3)$$

At the same time, we created a cloud mask and used an unsupervised classification algorithm (IsoCluster) to classify the ASTER image into five broad land cover categories: forest, bare soil, other vegetation, urban area and water.

DLST MODEL CALIBRATION

SIMULATION OF COARSE RESOLUTION BANDS

We created a grid with 990 m X 990 m cells, the same resolution as MODIS LST product, and excluded cells that overlapped with the cloud mask. This grid arrangement facilitated the integration of MODIS LST product with the bands of the three ASTER imaging subsystems: visible and NIR bands (15 m), SWIR (30 m) and Thermal Infra-Red (TIR) (90 m). In addition, we used this grid arrangement to resample the 14 ASTER bands by upscaling using the mean method; upscaling is the process whereby coarser resolution bands are computed from a higher resolution band.

Based on the original ASTER bands we calculated, for each 990 m cell, the following attributes: average UI, average NDVI, average NDWI, average radiance of TIR Band 13 ASTER, MODIS LST product value and each land cover class percentage.

RELATIONSHIP BETWEEN LST FROM MODIS PRODUCT AND RADIOMETRIC INDICES

We conducted exploratory analyses between the radiometric indices (UI, NDVI and NDWI) and LST from MODIS product. The Pearson correlation matrix indicated, with *p*-values smaller than 2.23×10^{-7}, that the three radiometric indices are highly correlated to LST MODIS product. Next, we selected all the cells with at least 80.0% of one land cover class, which resulted in a total of 101 selected cells. This selection process approaches the problem using the isothermal assumption, that

Revista Geoaraguaia
ISSN:2236-9716
Barra do Garças – MT
v.11 n. Esp. Geotecnologias
p. 07-33. Ago-2021

a pixel composed of only one material (i.e., land cover class) will have constant internal temperature variation.

Based on the 101 homogeneous cells we developed the following linear regression model:

$$\hat{T}_{990} = 16{,}17\ NDVI_{990} + 14{,}37\ NDWI_{990} + 47{,}80\ UI_{990} + 39{,}46 + u_i \quad (4)$$

Where:
$\hat{T}_{990}$= estimated temperature in Celsius degrees for a 990 m cell;
$NDVI_{990}$ = average NDVI for a 990 m cell;
$NDWI_{990}$ = average NDWI for a 990m cell;
UI_{990} = average UI for a 990m cell;
$39{,}46$ = model intercept;
u_i = random error.

The model achieved adjusted R^2= 0.73, residuals were normally distributed based on the Komolgorov-Smirnov normality test and the Breusch Pagan homoscedasticity test.

ESTIMATING EFFECTIVE EMISSIVITY AND ATMOSPHERIC RADIANCE CONTRIBUTION

In order to find the effective emissivity for each land cover class and the atmospheric radiance contribution, we considered the radiance registered by a sensor with its components, accordingly to the equation (5) defined by (LIU; PU, 2008):

$$R_s(i)_{990} = \sum_{k=1}^{K} \bar{\varepsilon}_k \cdot f_k(i)_{990} \cdot B_\lambda\left(T_k(i)\right)_{990} + R_A \quad (5)$$

Where:
$R_s(i)_{990}$ = radiance registered by ASTER band 13 sensor for a 990 m cell;
K = total number of land cover classes;
$\bar{\varepsilon}_k$ = Effective emissivity for land cover k;
$f_k(i)_{990}$ = k land cover percentage inside 990 m cell i;
$\left(T_k(i)\right)_{990}$= land surface temperature for land cover k inside 990 m cell i, from LST MODIS product;
$B_\lambda\left(T_k(i)\right)_{990}$= Thermal black body emittance for a given $T_k(i)$ of a 990 m cell;
R_A= Atmospheric radiance contribution.

Revista Geoaraguaia
ISSN:2236-9716
Barra do Garças – MT
v.11 n. Esp. Geotecnologias
p. 07-33. Ago-2021

$$R_s(i)_{990} = \sum_{k=1}^{K} \bar{\varepsilon}_k \cdot f_k\,(i)_{990} \cdot B_\lambda\left(T_k(i)\right)_{990} + R_A \quad (5)$$

Where:
$R_s(i)_{990}$ = radiance registered by ASTER band 13 sensor for a 990 m cell;
K = total number of land cover classes;
$\underline{\varepsilon}_k$ = Effective emissivity for land cover k;
$f_k\,(i)_{990}$ = k land cover percentage inside 990 m cell i;
$\left(T_k(i)\right)_{990}$= land surface temperature for land cover k inside 990 m cell i, from LST MODIS product;
$B_\lambda\left(T_k(i)\right)_{990}$= Thermal black body emittance for a given $T_k(i)$ of a 990 m cell;
R_A= Atmospheric radiance contribution.

First, we computed $B_\lambda\left(T_k(i)\right)_{990}$ for each 990 m cell. The B_λ parameter is calculated via Planck's law integration; we integrated Planck's law considering the temperature from LST MODIS product and the spectral range between 10.55 µm and 11.54 µm, the same range of MODIS 31 Thermal Band used to generate LST MODIS product. The Planck's law integration provides the total energy amount emitted by a blackbody in a given temperature, however the MODIS sensor does not detect the total amount. The energy is detected accordingly to the band spectral response curve, what means for MODIS 31 Thermal Band that 48.00% of the total energy amount is detected. Therefore, the radiance calculated with Planck's law integration was rescaled by a 0.48 multiplication factor. After this, we can rewrite Equation 5 as following:

$$R_s(i)_{990} = R_A + \sum_{k=1}^{K} \bar{\varepsilon}_k \cdot P_{k_{990}} \quad (6)$$

Where:
$R_s(i)_{990}$ = radiance registered by ASTER band 13 sensor for a 990 m cell;
R_A= Atmospheric radiance contribution;
$\bar{\varepsilon}_k$ = Effective emissivity for land cover k;
$P_{k_{990}}$ =$f_k\,(i).B_\lambda\left(T_k(i)\right)_{990}$, defined previously in Equation 5.

Equation 6 shows that the $R_s(i)_{990}$ variable is a linear combination of the other variables. Thus, we can say that each $\bar{\varepsilon}_k$ is an angular coefficient from this line and R_A is its linear coefficient.

Revista Geoaraguaia
ISSN:2236-9716
Barra do Garças – MT
v.11 n. Esp. Geotecnologias
p. 07-33. Ago-2021

Once $R_s(i)_{990}$ and $P_{k_{990}}$ are calculated for the 990 m cellular plan, we estimate R_A and ε_k (Table 4) using a linear regression model. All p-values were significant (< 0.001), and the model achieved an adjusted R^2= 0.84. Residuals were normally distributed based on the Komolgorov-Smirnov normality test and the Breusch Pagan homoscedasticity test.

Table 4 – Linear regression model parameters for $\hat{R}_A$ and $\hat{\varepsilon}_k$

Variable	Estimate	Standard deviation
R_A	4,44	0,77
$\bar{\varepsilon}_{Urban}$	0,74	0,09
$\bar{\varepsilon}_{Soil}$	0,75	0,10
$\bar{\varepsilon}_{Water}$	0,63	0,10
$\bar{\varepsilon}_{Other\ vegetation}$	0,67	0,10
$\bar{\varepsilon}_{Dense\ vegetation}$	0,69	0,10

Source: Authors (2021).

ESTIMATING THE THERMAL RADIANCE AT 90 M SPATIAL RESOLUTION

We generated a second grid arrangement with regular 90 m x 90 m cells. For each cell we calculated the following attributes: average UI, average NDVI, average NDWI, average radiance of TIR Band 13 ASTER and each land cover class percentage. Assuming that the relationships between the variables are independent of the scale, we applied the previously developed linear model (Equation 4) to each cell in the 90 m grid arrangement to obtain the temperature estimates at 90 m.

We applied Equation 5 to estimate a radiance value for each 90 m cell. After that, we calculated a linear regression between the estimated radiance and the original 90 m radiance from TIR Band 13 ASTER for each 90 m cell. This regression, by least squares method, allowed us to adjust the estimated values accordingly to Equation 7:

$$R_s(i)_{90} = 0{,}97.\overline{R_s(i)_{90}} + 0{,}25 \quad (7)$$

Where:

$R_s(i)_{90}$ = B13 ASTER original radiance 90 m;

$\overline{R_s(i)_{90}}$ = Estimated radiance for a 90 m cell in the cellular plan.

Revista Geoaraguaia
ISSN:2236-9716
Barra do Garças – MT
v.11 n. Esp. Geotecnologias
p. 07-33. Ago-2021

The model residuals are well-behaved and were approved (significance of 0.05) by the Kolmogorov-Smirnov normality test and the Breusch Pagan homoscedasticity test.

ESTIMATING THE THERMAL RADIANCE AT 15M SPATIAL RESOLUTION USING THE DLST MODEL

Assuming that the relationships between the variables are kept independently of the scale (ZHAN et al., 2013), we applied the calibrated DLST model for the original ASTER data to generate an estimated TIR Band 13 ASTER with 15 m spatial resolution.

IDENTIFICATION OF POTENTIAL SUHI AREAS

The radiance TIR Band 13 ASTER (90 m) and the Radiance TIR Band 13 estimated by the DLST model (15 m) were used as input to the emissivity reference channel technique, which assumes a single emissivity channel for all pixels in a band to calculate the land surface temperature (KEALY; HOOK, 1993). However, instead of using a single emissivity channel we chose to use one emissivity channel for each land cover class. The emissivity values for each class were defined through bibliographical research (JENSEN, 2006; NOVO, 2010; REES, 2001) as following: urban area = 0.95; bare soil = 0.90; water bodies = 0.92; forest = 0.98 and other vegetations = 0.97.

To assess the accuracy of the temperature estimate we subtracted the temperature extracted from the original TIR Band 13 ASTER (90 m) from the temperature extracted from estimated TIR Band 13 ASTER (90 m). We performed a visual comparison between the 15 m, 90 m and 990 m land surface temperature images in an area free of clouds in order to try to identify potential SUHI areas.

We also chose three further smaller study areas for a more detailed evaluation of the potential of the DLST model to identify SUHI effects. In order to numerically define urban heat island for the study area, we consulted meteorological temperature data for the image day at 10:00 and 11:00 am. As the ASTER satellite revisit time is at 10:30 am, we considered that the temperature increase is linear and calculated the average temperature between 10:00 and 11:00 am as a referential

temperature to compare with the images. This way, we subtracted 27.05ºC from the estimated DSLT temperature image (15 m), from the original ASTER temperature (90 m) and from the MODIS temperature (990 m); This was done in order to first make it easier to compare the three temperature images with different resolutions and second because we assume that temperatures above this constant value are a result of urban environment interference (this assumption is based on the fact that the meteorological station is located in a green area with perfect measurement conditions and that there is a correlation between air temperature and surface temperature).

RESULTS

DLST MODEL CALIBRATION AND APPLICATION FOR 15 M

After the adjustment our model performed R^2=0.66, i.e., approximately 66% of the variability of radiance B13 ASTER is explained by our estimated B13 ASTER (Figure 2). It is possible that the remaining 34% variability is related to other factors that were not considered in our linear regression model.

Figure 2 – Scatterplot of original B13 ASTER radiance X estimated B13 ASTER radiance. The red line represents the adjustment function. The axis unit is W/(m².sr.µm).

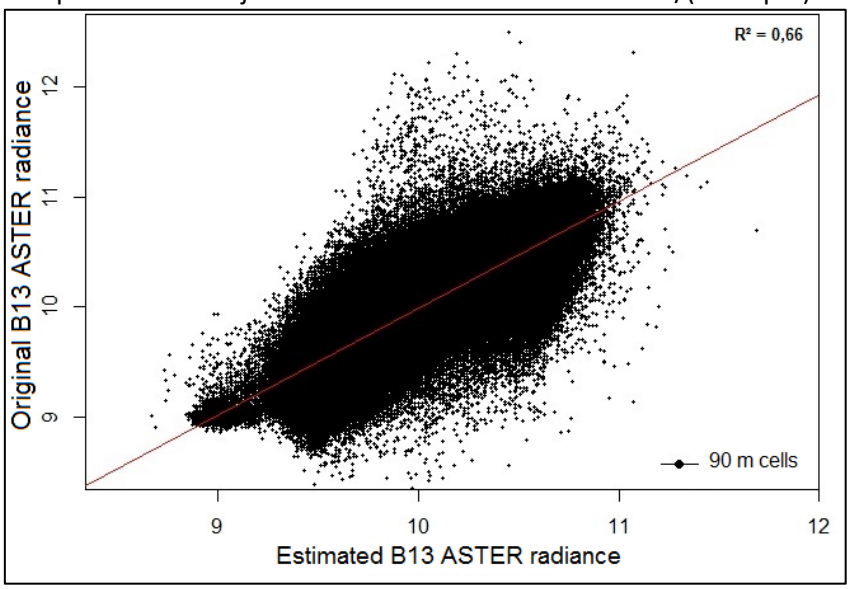

Source: Authors (2021).

The statistics of both images (Table 5) shows that the contrast (standard deviation) is smaller for estimated B13 ASTER radiance than for the original B13 ASTER radiance image, what is also seen in Figure 4. This lower variability occurs because the estimated image is based on radiometric indices that often saturate, i.e., after a certain reflectance value the index cannot distinguish the targets anymore and assigns the same value to targets with different intensity of urbanization, vegetation or water content. The same interference of radiometric indexes can be observed in the difference between Min and Max values.

Table 5 – Summary statistics of original B13 ASTER radiance and estimated B13 ASTER radiance. The unit is W/(m².sr.µm).

	Min	**1st quartile**	**Mean**	**3rd quartile**	**Max**	**Standard deviation**
B13 ASTER radiance	8.34	9.58	9.99	10.41	12.50	0.520
Estimated B13 ASTER radiance	8.66	9.59	9.96	10.35	11.59	0.421

Source: Authors (2021).

In order to evaluate the model behaviour for each land cover class, we summarized statistics with boxplots (Figure 3) for all land cover classes for original B13 ASTER radiance (B13) and estimated B13 ASTER radiance (DLST).

Figure 3 – Boxplots for estimated B13 ASTER radiance (DLST) and original B13 ASTER (B13) radiance image for each land cover class. The dashed line is the mean and the continuous line is the median.

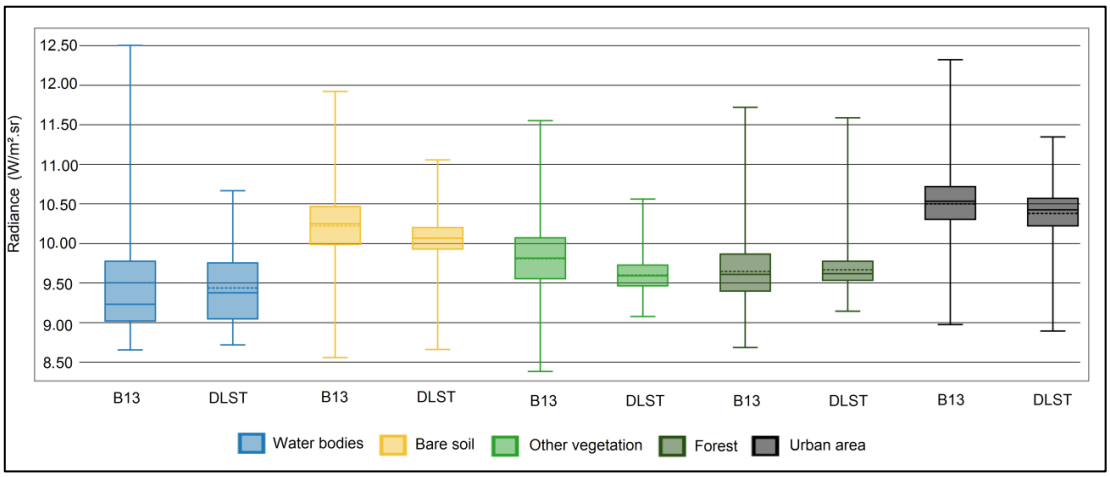

Source: Authors (2021).

All classes showed a compression in variability compared to the original B13 ASTER (B13) radiance, mainly in the upper limits of the respective distribution. This data compression is characteristic of saturated images and is common in radiometric indices. The water class showed similar statistics to the original B13 ASTER (B13) radiance, except for the lower variability in the 4th quartile, which may have occurred due to NDWI saturation. The bare soil class showed more considerable differences, with more intense variability compression of the whole data. This probably occurred because we did not use any specific radiometric indices for this land cover class (although it has spectral similarity to urban areas the UI is not the best way to represent this class). Both vegetation classes showed considerable differences in all statistics, except for the mean. All other statistics differ for more than 0.15 W/(m².sr.µm) from the original values. Considering that NDVI saturates due to leaf area index, atmospheric interferences, water content, view angle and other factors; it was expected that the estimated values for these classes would be more inaccurate, and the results confirm this. The urban class showed very similar statistics values: the largest difference between the original and estimated value was 0.97 W/(m².sr.µm) for maximum value.

Based on these results, the DLST model was considered adequate, in particular for the urban class which is the main target of this work and had the best DLST model performance. At 15 m spatial resolution, the model showed a good visual performance increasing the visible details, while however also generating some artefacts and a salt and pepper effect in certain locations. Figure 4 shows the radiance images generated by the DLST model: upscaled 990 m, DLST 90 m and DLST 15 m and the original ASTER radiance 90 m.

LST EXTRACTION AND IDENTIFICATION OF POTENTIALS SUHI AREAS

The subtraction between the temperature extracted from original TIR Band 13 ASTER (90 m) and the temperature extracted from estimated TIR Band 13 ASTER (90 m) indicated that the temperature differences ranged from -5.60 ºC to 5.80 ºC. The largest negative differences were concentrated within vegetation classes, while the largest positive differences were concentrated within the bare soil class and the urban area class, show in differences from -1.99 ºC to 4.00 ºC.

The subtraction of 27.05 ºC from each temperature image allowed a better visualization of the potential SUHI areas in our study area. Figure 5 shows this at three different scales and levels of detail. The MODIS LST 990 m image generalized almost the whole area in the 7.56 ºC to > 9.72 ºC range, with no intraurban temperature details; the LST ASTER 90m image allowed the visualization of some details for different urban regions, ranging from 1.94 ºC to 7.20 ºC; the DLST model 15 m image enabled the visualization of details inside urban regions, for transition areas between land cover classes and for smaller intraurban areas with lower temperatures. In addition, with the DLST model 15 m image is possible to point out some more intense potential SUHI areas.

Figure 4 – B13 upscaled radiance 990 m, B13 original ASTER radiance 90 m, estimated B13 ASTER radiance 90 m and estimated B13 ASTER radiance 15 m.

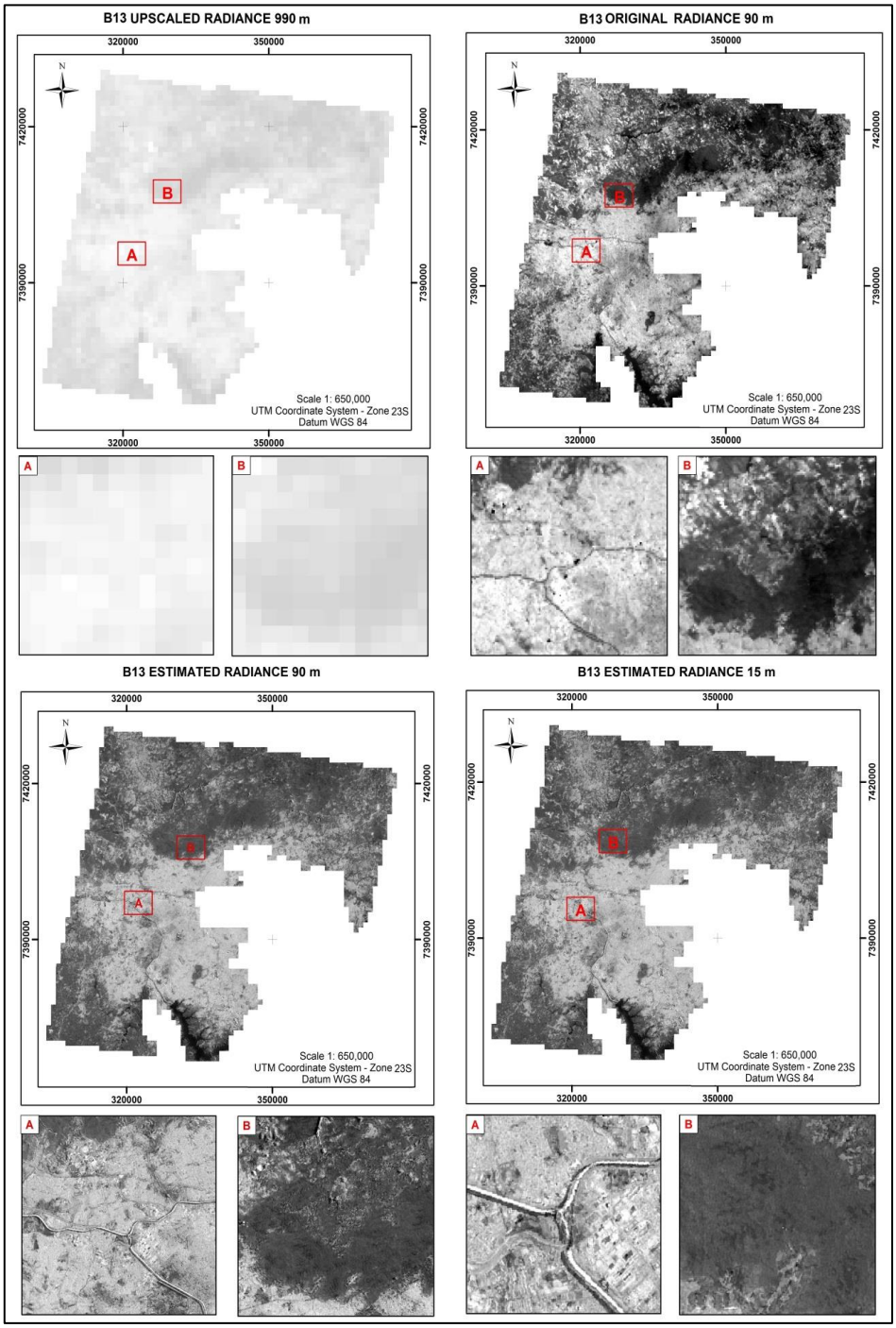

Source: Authors (2021).

Figure 5 – LST MODIS 990 m extracted from LST MODIS product; LST ASTER 90m extracted from B13 original ASTER radiance 90 m; DLST model 15 m extracted from estimated B13 ASTER radiance 15 m.

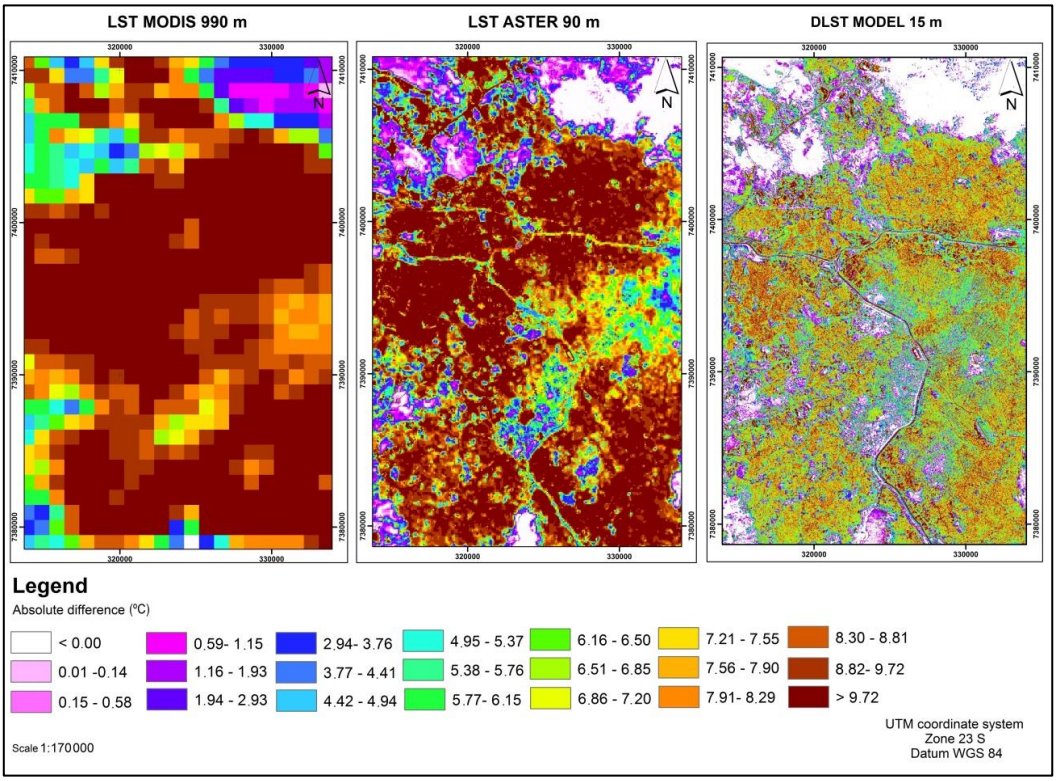

Source: Authors (2021).

In order to further analyse the behaviour of the DLST model 15 m, we identified three potential SUHI areas and explored these using the LST ASTER 90m extracted, DLST model 15 m and ASTER composite bands R(3)G(2)B(1). The LST MODIS 990 m image was not considered because, as shown in Figure 5, it is too coarse for this purpose.

In most of the first selected area (Figure 6), Morumbi neighbourhood, temperatures are more pleasant than in its surrounding. This effect is due to a high arborisation rate, the larger spacing between built-up areas and its location within the route of the most frequent and intense winds in this area. The Paraisópolis favela (marked with a black circle in Figure 6) is nearby Morumbi and it was already identified as an SUHI area by (FUCKNER, 2008). Compared to the LST ASTER 90m image, the DLST MODEL 15 m allows the visualization of temperature variations within Paraisópolis

and a surrounding damping zone, which is due to the vegetation in Morumbi neighbourhood. The DLST model 15 m was able to capture the effect of the distinct urbanization patterns on LST. Distinct urbanization patterns here are understood as the different materials used for construction, urban geometric arrangements, arborisation rates and land use.

Figure 6 – LST for Morumbi neighbourhood and Paraisópolis shantytown (black circle), the scale is 1: 70000.

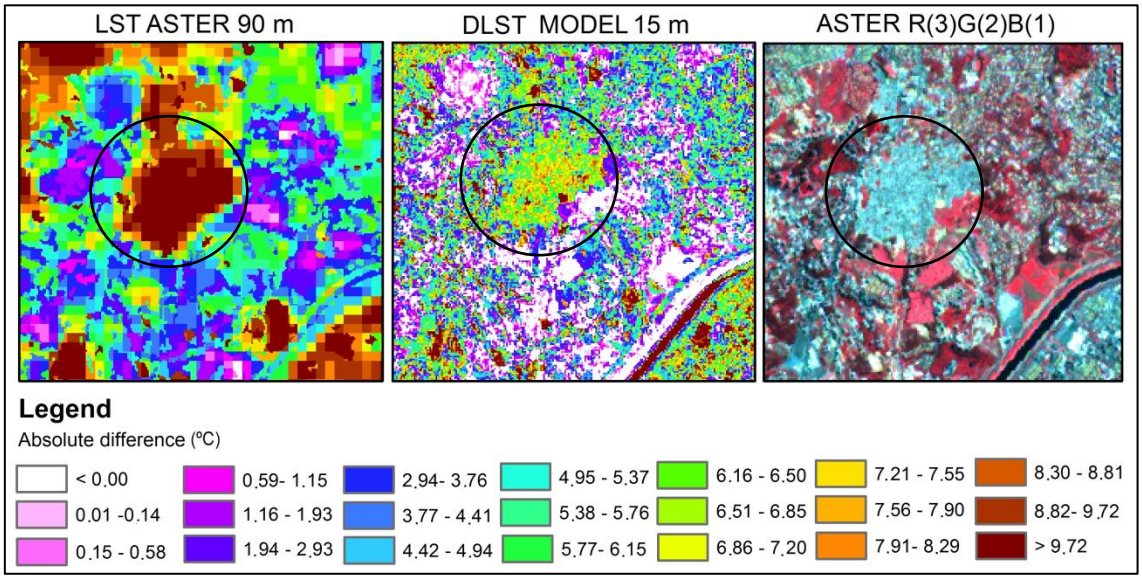

Source: Authors (2021)

Vila Leopoldina neighbourhood (Figure 7) shows only high temperatures in the LST ASTER 90m image, (more than 9.72 ºC above the reference temperature of 27.05 ºC). The DLST model 15m however shows that the high temperatures are concentrated on an industrial complex area (marked with a black circle in figure 7). In this area roofs are made from materials that preserve the heat (e.g. metallic roofs and roofs constructed from asbestos).

Figure 7 – LST for Vila Leopoldina neighbourhood and its industrial complex area (black circle), the scale is 1: 70000.

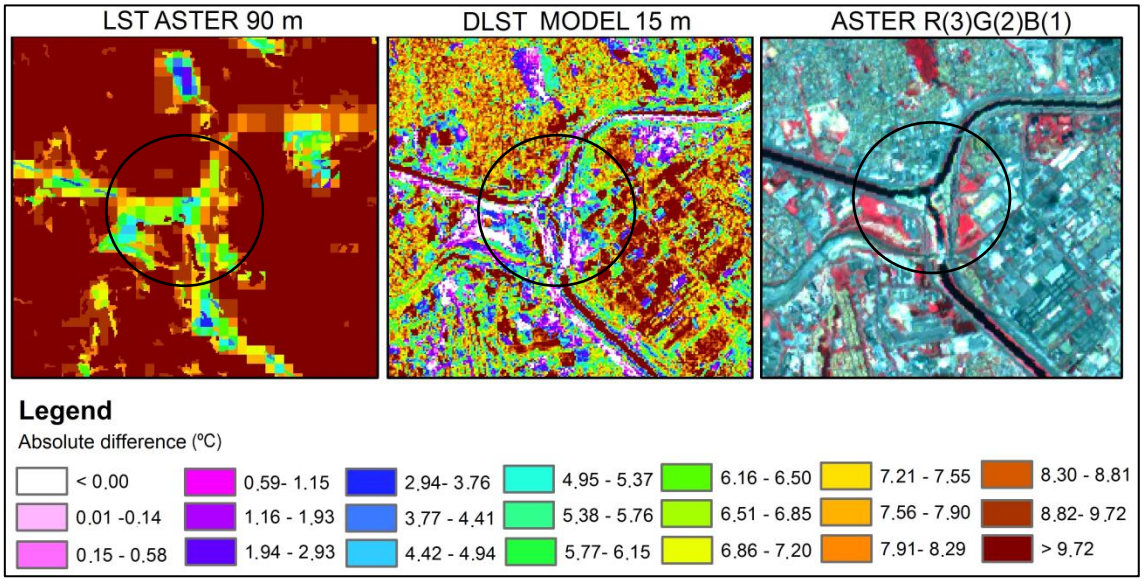

Source: Authors (2021).

In the area around the Paulista avenue (marked with a black ellipse in Figure 8) the DLST model identified temperature variations caused by the verticalized and high urban density area, which creates an urban canyon surrounding the avenue. The parallel traces of the streets in conjunction with the canyon formed by the buildings create windy corridors. This causes that the wind passes through the streets at ground level, without moving the layer of hot air located just above the verticalized built-up area. This effect contributes to the consequent temperature increase.

Figure 8 – LST for Paulista Avenue (black ellipse) and its neighbourhood, the scale is 1: 70000.

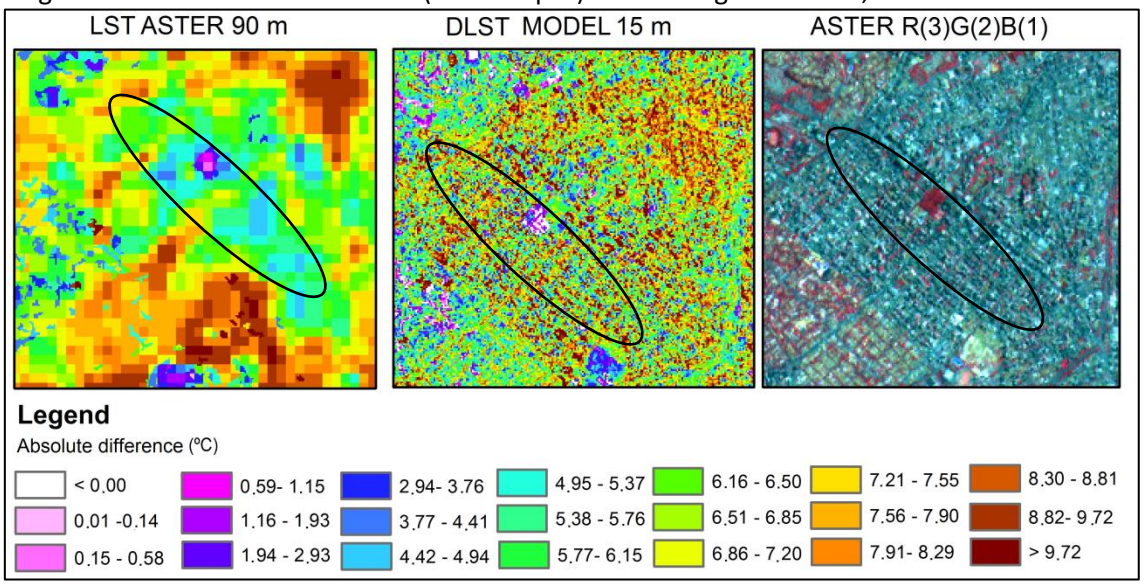

Source: Authors (2021)

CONCLUSIONS

The main objective of this research was to use a DLST model based on linear regression to generate more detailed LST images for urban areas and consequently be able to perform more detailed analyses on urban surface temperature patterns and SUHI. The main advantages of the use of linear regression to develop the DLST model are its low computational cost and possibility to perform further quantitative analyses of the accuracy of the resulting LST estimates.

Despite the inaccuracies in estimation of the radiance, the model was capable of providing details about the intraurban land surface temperature. In addition, the model was able to represent the intensity variations of SUHI's which correspond to the urbanization pattern, the presence of vegetation and the thermal specifications of roof materials (in particular for industrial buildings).

The analysis of the results showed that the proposed methodology has potential to support identification of intraurban SUHI areas. The DLST model achieved $R^2 = 0.66$ for a 3900 km^2 study area with large variability in land cover and atmospheric conditions. While this is less than certain

previous studies (LIU; PU, 2008; LIU; ZHU, 2012) which report an R^2 between 0.77 and 0.82, it should be noted that our study area is approximately six times larger than study areas in these studies.

We tested the method to identify the LST in different regions of our study area. Estimates were most accurate for the urban land cover class. The DLST 15 m image was able to identify details that the LST ASTER 90 m image could not is therefore an improvement for identification of SUHI areas. In addition, the DLST 15 m image contribute to the identification of diverse temperature patterns associated with a specific urbanization pattern.

For future research we recommend to explore: (1) more images, in order to analyse the seasonality of surface intraurban heat island; (2) more radiometric indexes which could represent other variables that impact land surface temperature and this way improve the DLST model estimation.

It is also highly recommended the acquisition of a thermal image with spatial resolution compatible to the final estimated image (15 m), in order to compare the model estimative with a ground truth thermal image. This way, instead of assuming that the relationships are kept independently of the scale, it would be possible to verify these relationships between more similar scales to check this premise.

Another point to be explored is the application of DLST model on Landsat 8 images; as the Landsat 8 and MODIS coverages are asynchronous, it is not possible to disaggregate Landsat 8 thermal data based on MODIS LST product. Thus, another alternative is required to realize this experiment, probably a thermal aero survey.

It is important to highlight that this DLST model can be replied with orbital images of other satellites as: Landsat series, NOAA, AVHRR, since there is auxiliary data available and a LST product as reference.

REFERENCES

ADLER-GOLDEN, S. M. et al. Atmospheric Correction for Short-wave Spectral Imagery Based on MODTRAN 4, in: **Imaging Spectrometry V**, 1999, vol. 3753, no. July, pp. 61–69.

ANIELLO C.; MORGAN, K.; NEWLAND, L. Micro-urban heat island landsat TM and a GIS using, **Comput. Geosci.**, vol. 21, no. 8, p. 4, 1995.

AZEVEDO, T. S. et al Ilhas de calor e aedes aegypti : um estudo preliminar para a cidade de Santa Bárbara d ' Oeste , sp – Bra , utilizando sensoriamento remoto, *in*: **I Congreso Latinoamericano de Ecología Urbana " Desafíos y escenarios de desarrollo para las ciudades latino-americanas"** , 2012, pp. 174–185.

BECHTEL, B.; BÖHNER, J.; WIESNER, S. **Downscaling of diurnal land surface temperature cycles for urban heat island monitoring,** pp. 91–94, 2013.

BOGGIONE, G. A. et al, Simulation of a Panchromatic Band by Spectral Combination of Multispectral ETM + Bands, *in*: **International Symposium on Remote Sensing of Environment (ISRSE)**, 2003, pp. 4–6.

CLIMATE PROTECTION PARTNERSHIP, **Reducing Urban Heat Islands : Compendium of Strategies Urban Heat Island Basics**, USA, 2010.

CROW, W. T.; WOOD, E. F., **The assimilation of remotely sensed soil brightness temperature imagery into a land surface model using Ensemble Kalman filtering : a case study based on ESTAR measurements during SGP97**. vol. 26, no. 2003, pp. 137–149, 2005.

DENNISON, P. et al. Wildfire temperature and land cover modeling using hyperspectral data, **Remote Sens. Environ.**, vol. 100, no. 2, pp. 212–222, Jan. 2006.

DOMINGUEZ, A. et al. High-resolution urban thermal sharpener (HUTS), **Remote Sens. Environ.**, vol. 115, no. 7, pp. 1772–1780, Jul. 2011.

ECKMANN, T.; ROBERTS, D.; STILL, C. Using multiple endmember spectral mixture analysis to retrieve subpixel fire properties from MODIS **Remote Sens. Environ**., vol. 112, no. 10, pp. 3773–3783, Oct. 2008.

EFRAIN, A., B. et al. **Urban Heat Island development during the last two decades in Porto Alegre, Brazil and its monitoring**, pp. 61–64, 2013.

FUCKNER, M. A., Aplicação de imagens ASTER no estudo do ambiente urbano de São Paulo e Rio de Janeiro, São José dos Campos: INPE, 2008.

GALLO, K. P. et al. Assessment of urban heat islands: a satellite perspective, **Atmos. Res.,** vol. 37, no. 1–3, pp. 37–43, Jul. 1995.

GAO, B. NDWI—A normalized difference water index for remote sensing of vegetation liquid water from space, **Remote Sens. Environ**., vol. 58, no. 3, pp. 257–266, Dec. 1996.

GARTLAND, L. *Heat Island: Understanding and mitigating heat in urban areas*. London: **EarthScan**, 2008, p. 215.

HAJAT, S.; KOSATKY, T. Heat-related mortality: a review and exploration of heterogeneity, **J. Epidemiol. Community Health**, vol. 64, no. 9, pp. 753–60, Sep. 2010.

HOWARD, L., **The climate of London deduced from meteorological observations, made at different places in the neighbourhood of the metropolis**. Londres: W.Philips&G.Yards, 1820, p. 410.

IBGE, **Síntese dos indicadores sociais: Uma análise das condições de vida da população brasileira 2010**, Rio de Janeiro: IBGE, 2010.

JAYAMANNA S., Relation Between Social and Environmental Conditions in Colombo. Sri Lanka and the Urban Index Estimated by Satellite Remote Sensing Data, **Int. Arch. Photogramm**. **Remote Sens**., vol. XXXI, no. B7, pp. 321–326, 1996.

JENSEN, J. R., **Remote Sensing of the Environment: An Earth Resource Perspective**, 2ª ed. Englewood Cliffs: Prentice Hall, 2006, p. 592.

KAWASHIMA, S. Relation between Vegetation, Surface Temperature, and Surface Composition in the Tokyo Region during Winter, **Remote Sens. Environ**., vol. 60, no. April, pp. 52–60, 1994.

KEALY, P. S.; HOOK, S. J. Separating Temperature and Emissivity in Thermal Infrared Multispectral Scanner Data: Implications, **IEEE Trans. Geosci. Remote Sens**., vol. 31, no. 6, pp. 1155–1164, 1993.

KUSTAS W.; ANDERSON M. Advances in thermal infrared remote sensing for land surface modelling **Agric. For. Meteorol**., vol. 149, no. 12, pp. 2071–2081, Dec. 2009.

LIU, D.; PU, R., **Downscaling Thermal Infrared Radiance for Subpixel Land Surface Temperature Retrieval**, pp. 2695–2706, 2008.

LIU, D.; ZHU, X., An Enhanced Physical Method for Downscaling Thermal Infrared Radiance, *IEEE* **Geosci. Remote Sens. Lett**., vol. 9, no. 4, pp. 690–694, Jul. 2012.

LOMBARDO, M. A. **Ilha de Calor nas Metrópoles**, vol. 16, no. 1. São Paulo: Hucitec, 1985, p. 244.

MCLAUGHLIN, D., An integrated approach to hydrologic data assimilation: interpolation, smoothing, and filtering, **Adv. Water Resour**., vol. 25, no. 8–12, pp. 1275–1286, Aug. 2002.

MCMICHAEL A. J. et al. International study of temperature, heat and urban mortality: the 'ISOTHURM' project., **Int. J. Epidemiol.,** vol. 37, no. 5, pp. 1121–31, Oct. 2008.

MENDONÇA, F.; DANNI-OLIVEIRA, I. M. **Climatologia: Noções básicas de climas do Brasil**. São Paulo: Oficina de Textos, 2007, p. 206.

MERLIN O. et al. **Multidimensional Disaggregation of Land Surface and Microwave-L Bands** vol. 50, no. 5, pp. 1864–1880, 2012.

MEMON, R. A.; LEUNG, D. Y. C.; CHUNHO, L., A review on the generation, determination and mitigation of urban heat island. **J. Environ. Sci.** *(China)*, vol. 20, no. 1, pp. 120–8, Jan. 2008.

MONTEIRO, C. A. F. **Teoria e Clima Urbano**. São Paulo: USP, 1976.

NICHOL, J.; WONG, M. S. Mapping urban environmental quality using satellite data and multiple parameters, **Environ. Plan. B Plan. Des.**, vol. 36, no. 1, pp. 170–185, 2009.

NOVO, E. M. L. de M., **Sensoriamento remoto: princípios e aplicações**, 4ª ed. São Paulo: Blucher, 2010, p. 387.

OGASHAWARA, I.; BASTOS V. B., A Quantitative Approach for Analyzing the Relationship between Urban Heat Islands and Land Cover, **Remote Sens**., vol. 4, no. 12, pp. 3596–3618, Nov. 2012.

OKE, T. R. **Boundary Layer Climates**, 2nd ed. London: Methuen, 1987, p. 435.

REES, W. G. **Physical Principles of Remote Sensing**, 2ª ed. Cambridge: Cambrydge University Press, 2001, p. 369.

ROTH, M.; OKE, T. R. Satellite-derived urban heat island from three coastal cities and and the utilization of such data in urban climatology, **Int. J. Remote Sens**., vol. 10, no. 11, pp. 1699–1720, 1989.

ROUSE, J. W. et al., Monitoring vegetation systems in the Great Plains with ERTS, in: **Third ERTS Symposium**, 1973, vol. 1, pp. 309–317.

SZYMANSKI, J. J. et al. **Subpixel temperature retrieval with multispectral sensors**, vol. 3717, no. 1981, 1999.

TAN, J. et al. The urban heat island and its impact on heat waves and human health in Shanghai, **Int. J. Biometeorol**., vol. 54, no. 1, pp. 75–84, Jan. 2010.

VOOGT, J.; OKE, T. Thermal remote sensing of urban climates, **Remote Sens. Environ.,** vol. 86, no. 3, pp. 370–384, Aug. 2003.

WANG, G.; HE, G.; LIU, J. **A New Classification Method for High Spatial Resolution Remote**, pp. 186–190, 2012.

YANG G. et al. A Novel Method to Estimate Subpixel Temperature by Fusing Solar-Reflective and Thermal-Infrared Remote-Sensing Data with an Artificial Neural Network, **IEEE Trans. Geosci. Remote Sens.**, vol. 48, no. 4, pp. 2170–2178, Apr. 2010.

ZAKŠEK, K.; OŠTIR, K. Downscaling land surface temperature for urban heat island diurnal cycle analysis, **Remote Sens. Environ**., vol. 117, pp. 114–124, Feb. 2012.

ZHAN, W. Disaggregation of remotely sensed land surface temperature: Literature survey, taxonomy, issues, and caveats, **Remote Sens. Environ**., vol. 131, no. 19, pp. 119–139, Apr. 2013

ZHOU J. et al. Maximum Nighttime Urban Heat Island (UHI) Intensity Simulation by Integrating Remotely Sensed Data and Meteorological Observations, ***IEEE J. Sel. Top. Appl. Earth Obs. Remote Sens.***, vol. 4, no. 1, pp. 138–146, Mar. 2011.